Comparison of Global Martian Plasma Models in the Context of MAVEN Observations

Hilary Egan[1], Yingjuan Ma[2], Chuanfei Dong[3], Ronan Modolo[4], Riku Jarvinen[5,10], Stephen Bougher[6], Jasper Halekas[7], David Brain[1], James McFadden[8], Jack Connerney[9], David Mitchell[8], Bruce Jakosky[1]

[1]University of Colorado, Boulder CO, USA

[2]University of California Los Angeles, Los Angeles CA, USA

[3]Princeton University, Princeton NJ, USA

[4]LATMOS/IPSL, UVSQ Universite Paris-Saclay, UPMC University Paris CNRS, Guyancourt, France

[5]Finnish Meteorological Institute, Helsinki, Finland

[6]University of Michigan, Ann Arbor MI, USA

[7]University of Iowa, Iowa City IA, USA

[8]SSL/University of California Berkeley, Berkeley CA, USA

[9]NASA/Goddard Space Flight Center, Greenbelt MD, USA

[10]Department of Electronics and Nanoengineering, School of Electrical Engineering, Aalto University, Espoo, Finland

Corresponding author: H. Egan, hilary.egan@colorado.edu

Abstract

Global models of the interaction of the solar wind with the Martian upper atmosphere have proved to be valuable tools for investigating both the escape to space of the Martian atmosphere and the physical processes controlling this complex interaction. The many models currently in use employ different physical assumptions, but it can be difficult to directly compare the effectiveness of the models since they are rarely run for the same input conditions. Here we present the results of a model comparison activity, where five global models (single-fluid MHD, multi-fluid MHD, multi-fluid electron pressure MHD, and two hybrid models) were run for identical conditions corresponding to a single orbit of observations from the Mars Atmosphere and Volatile EvolutioN (MAVEN) spacecraft.

We find that low altitude ion densities are very similar across all models, and are comparable to MAVEN ion density measurements from periapsis. Plasma boundaries appear generally symmetric in all models and vary only slightly in extent. Despite these similarities there are clear morphological differences in ion behavior in other regions such as the tail and southern hemisphere. These differences are observable in ion escape loss maps, and are necessary to understand in order to accurately use models in aiding our understanding of the martian plasma environment.

1 Introduction

Mars presents a richly complicated and time variable obstacle to the solar wind, consisting of both a conducting ionosphere and localized crustal magnetic fields, but no global dipole field. The interaction region between the undisturbed solar wind and the lower ionosphere hosts a wide variety of physical processes and plays an important role in the energization of planetary particles, atmospheric escape, and upper atmospheric phenomena such as aurora.

Computer models can greatly assist our understanding of these physical processes when used in conjunction with data. The first models of Martian gas dynamics were *Spreiter et al.* [1970] and *Dryer and Heckman* [1967]. Since then the number of models capable of simulating the Martian magnetosphere has proliferated greatly, and now includes a variety of MHD [*Ma et al.*, 2015; *Dong et al.*, 2015; *Najib et al.*, 2011; *Terada et al.*, 2009; *Harnett and Winglee*, 2007], Hybrid [*Brecht et al.*, 2016; *Kallio and Janhunen*, 2002; *Boesswetter et al.*, 2010; *Modolo et al.*, 2016; *Holmstrom and Wang*, 2015; *Jarvinen et al.*,

2018], and test particle [*Cravens et al.*, 2002; *Fang et al.*, 2008; *Liemohn et al.*, 2013] models.

These models have been used to understand an extensive array of Martian plasma processes and interactions. Plasma boundaries [*Najib et al.*, 2011; *Bertucci et al.*, 2005; *Bößwetter et al.*, 2004], spatial ion distribution [*Najib et al.*, 2011], ion escape [*Brecht et al.*, 2016; *Brecht and Ledvina*, 2014; *Dong et al.*, 2015b; *Kallio et al.*, 2006a; *Fang et al.*, 2010], magnetic topology [*Liemohn et al.*, 2006] energetic neutral atoms (ENAs) [*Kallio et al.*, 2006b; *Gunell et al.*, 2006; *Wang et al.*, 2016, 2014], solar wind alpha particles [*Chanteur et al.*, 2009], and X-ray emission [*Gunell et al.*, 2004] have all been studied using Martian plasma models. Transient processes including CMEs [*Ma et al.*, 2017; *Dong et al.*, 2015a], changes in dynamic pressure [*Ma et al.*, 2014], changes in solar EUV flux [*Modolo et al.*, 2006; *Modolo et al.*, 2005], seasonal variation [*Dong et al.*, 2015], and crustal field rotation [*Ma et al.*, 2014; *Fang et al.*, 2015] have also been topics of study. Long term Martian evolution has also been examined through estimation of early conditions and the corresponding escape rates [*Terada et al.*, 2009].

The wide variety of models presents a unique challenge in cross-validation of results. In addition to different implementations and numerical methods, each model type makes different implicit physical assumptions. This means that the study of a particular plasma process may be more or less valid with the use of a particular model. The strengths and weaknesses of various models have been discussed previously in the literature [*Ledvina et al.*, 2008]. Directly comparing model results provides a complementary approach to the aforementioned discussion, to determine how the fundamental differences affect the interpretation of simulations.

Here we perform a model comparison challenge where we run a variety of models with the same input conditions to understand the strengths and weaknesses of each one. Running a model challenge allows the comparison across a variety of model types in a one-to-one manner and isolates the effects of different physics from the effects of the input conditions.

Model challenges are a commonly used tool across a variety of disciplines (e.g. *Kim et al.* [2016], *Hurrell* [1995]). Within the Martian modelling community, one such model challenge has previously been performed [*Brain et al.*, 2010]; however, substantial model development has occurred in the interim, and it is useful to provide an updated ef-

79 fort and expand the types of analysis performed. Here we evaluate different quantities, be-

80 yond boundaries and global escape rates. Additionally we compare to Mars Atmospheric

81 Volatile EvolutioN (*Maven*) [*Jakosky et al.*, 2015] data from a single orbit with upstream

82 conditions that correspond to our model inputs. This provides a baseline measurement for

83 comparison in the region of the spacecraft orbit. In particular, *Maven* adds critical infor-

84 mation due to its simultaneous measurements of particles and fields.

85 In this paper we report the results from such a model comparison challenge. We

86 identified a suitable *Maven* orbit, extracted the upstream solar wind drivers, and ran a va-

87 riety of models using nearly identical input conditions. In Section 2 we describe the input

88 conditions and codes. Our results are shown in Section 3, where we focus on the plasma

89 boundaries (3.1), low altitude ion behaviour (3.2), southern hemisphere (3.3), and global

90 escape (3.4). We conclude with a discussion and summary in Section 4, as well as brief

91 projection of our future work.

2 Methods

2.1 Orbit

94 This model challenge was designed such that the results can be compared to data

95 from a specific MAVEN orbit. The trajectory of the chosen orbit (#2349, 2015/12/14) is

96 depicted in Fig. 1. The coordinates are labeled in the Mars Solar Orbital (MSO) coordi-

97 nate system; $+\vec{x}$ is the direction from Mars to the sun, $+\vec{z}$ is perpendicular to the orbital

98 plane of Mars, and $+\vec{y}$ is the completion of a right-handed coordinate system. This orbit

99 is almost entirely in the terminator plane, with periapsis near dawn at the equator. The

100 sub-solar longitude is 170°, indicating that the dominant crustal fields are on the dayside

101 of the planet as the dominant crustal fields are centered around a geographic longitude of

102 180°.

103 Fig. 1 also shows data from the Solar Wind Electron Analyzer (SWEA) [*Mitchell*

104 *et al.*, 2016], Solar Wind Ion Analyzer (SWIA) [*Halekas et al.*, 2015], Suprathermal and

105 Thermal Ion Composition (STATIC) [*McFadden et al.*, 2015], and the Magnetometer (MAG)

106 [*Connerney et al.*, 2015] rotated into MSO coordinates. *Maven* exits and enters the up-

107 stream solar wind at times 17:12 and 20:24 respectively. At times 17:30-18:30 both STATIC

108 and SWIA show a group of highly energetic ions whose energy increases with altitude in

109 the northern hemisphere, commonly refered to as the ion plume. Periapsis occurs around

113 **Figure 1.**   Trajectory and data from the *Maven* orbit (2349, 12/14/2015) that the upstream conditions are

114 drawn from. *Left:* Panels show a) electron flux per energy as measured by SWEA, b) ion flux per energy

115 as measured by SWIA, c) ion flux per energy as measured by STATIC, d) ion flux per mass as measured by

116 STATIC, e) and magnetic field as measured by MAG. The x-axis is labeled by time, altitude, and Solar Zenith

117 Angle (SZA). *Right:* Trajectory of *Maven* orbit in MSO coordinates. Empirical boundaries [*Trotignon et al.*,

118 2006] are plotted as dashed lines, and the color corresponds to the time bar on the left.

125 **Table 1.**   Upstream conditions and derived parameters extracted from *Maven* data, used to drive the models.

126 Here P_{dyn} is the dynamical pressure and v_A is the Alfven speed.

v	$[-350, 0, 0]$ km/s
n_p	4.9 cm^{-3}
n_α	0.14 cm^{-3}
T_p	59200 K
B	$[-0.74, 5.46, -0.97]$ nT
P_{dyn}	0.5 nPa
v_A	55 km/s

110 18:43 where many heavy ions are measured. The outbound portion of the orbit shows an-

111 other section of heavy ions from times 19:05-19:25. The model results for these regions

112 will be explored in Section 3.

119 ### 2.2 Upstream Boundary

120 The upstream boundary conditions (Table 1) were calculated from period of orbit

121 #2349 *Maven* is in the upstream solar wind, and are listed in Table 1. These conditions

122 are relatively moderate, not representing an extreme event, and are consistent between the

123 inbound and outbound portion of the orbit. The interplanetary magnetic field (IMF) is

124 almost entirely in the $+\vec{y}$ direction, perpendicular to the solar wind velocity.

127 ### 2.3 Models

128 As shown in Table 2, a wide variety of models were run for this model challenge,

129 with different codes and underlying physical assumptions. Each model will be referred

130 to by the tag given in the first column to minimize confusion between similar models. In

5

	Model type	Crustal Fields	Highest Resolution (km)	Inner Boundary (km)
BATSRUS-MS [1]	MHD	Yes	10	100
BATSRUS-MF [2]	MHD	Yes	10	100
BATSRUS-MF+PE [3]	MHD	Yes	10	100
HELIOSARES [4]	Hybrid	Yes	60	110
RHybrid [5]	Hybrid	No	113	300

Table 2. A summary of the models used in this model challenge along with some of the relevant parameters. For reference, scale heights for O^+, O_2^+, and CO_2^+ are 40 km, 20 km, and 10 km, respectively. (1) *Ma et al.* [2004], (2) *Najib et al.* [2011], (3) *Ma et al.* [2013], (4) *Modolo et al.* [2016], (5) *Jarvinen et al.* [2018]

this section we describe the models, some of the relevant implementation details, and any differences in the parameters used to run the simulations. Although multiple crustal field models were used, this will not cause a significant difference in the results.

2.3.1 MHD Models

The three magnetohydrodynamics (MHD) models were all run within the BATS-R-US (Block Adaptive-Tree Solar wind Roe-type Upwind Scheme) code [*Ma et al.*, 2004; *Glocer et al.*, 2009; *Najib et al.*, 2011]. The BATS-R-US platform has a non-uniform spherical grid to maximize resolution near the planet while minimizing computation time. The radial resolution varies from 10 to 600 km, and the angular resolution varies between 1.875 and 3.75. The simulated domain extends from -24 to +8 R_M (where R_M is the radius of Mars) in the x-direction, and -16 to +16 in the y and z directions. Local time stepping is utilized such that the time step can vary dynamically between cells while satisfying the Courant condition.

Within this platform, 3 separate simulations were performed with increasing complexity. The first, BATSRUS-MS [*Ma et al.*, 2004], is a multi-species run where ions H^+, O^+, O_2^+, and CO_2^+ were included and treated as a single fluid. This model solves a single momentum and energy equation but separate continuity equations for each species. BATSRUS-MF, the second model [*Najib et al.*, 2011], includes the same ion species but each each species is treated as a separate fluid with its own continuity and momentum equations. BATSRUS-MF+Pe [*Ma et al.*, 2013] includes the same ion species as indepen-

dent fluids, and also solves an equation for the electron pressure analogous to the energy equation that dictates ion pressure (see details in *Ma et al.* [2011]), allowing the electron temperature to differ from the ion temperature.

For all three simulations the lower boundary of the code is set at 100 km above the planet, and the O^+, O_2^+, and CO_2^+ densities are set by the photo-equilibrium values. The velocity condition at the lower boundary is reflexive, leading to an approximately zero value. Crustal fields were included as modeled by *Arkani-Hamed* [2001].

2.3.2 Hybrid Models

The two hybrid simulations were run using two different codes: HELIOSARES [*Modolo et al.*, 2016], and RHybrid [*Jarvinen et al.*, 2018]. As hybrid codes they both treat ions as macroparticles that evolve kinetically according to the Lorentz force, while the electrons are implemented as a charge neutralizing fluid. A macroparticle does not represent a single physical particle, rather a group of particles with a given density and the same properties. Fields are advanced by accumulating particle moments according to macroparticle shape functions onto a grid using a cloud-in-cell technique and then solving the magnetic and electric field equations accordingly. In order to improve particle statistics, multiple independent time steps were averaged together to create the datasets that were analysed here. Both models include planetary H^+, O^+, and O_2^+, He^{++}, and H^+. Although CO_2+ is included in the HELIOSARES simulation, due to the limited resolution compared to the ion scale height it is not included in further analysis. The RHybrid run analyzed here does not include CO_2+.

This HELIOSARES run uses a cartesian grid with a resolution of 60 km, and a lower boundary at 110 km, and bounds $X = [-2.7R_M, 2.1R_M]$, $Y, Z = \pm4.7R_M$. Crustal fields are included via the *Cain et al.* [2003] model. HELIOSARES also implements a particle splitting technique to limit numerical noise that results from having large particles; when a macroparticle with a statisical weight ≥ 3 times the solar wind density exceeds 700 km in altitude, it is split into two child particles with the same velocity and half the statistical weight. Solar wind and ionospheric electrons are modelled as two separate fluids, with densities set by the solar wind ion density and ionospheric ion density respectively. The solar wind electron population is assumed to be adiabatic with polytropic index $\gamma_{sw} = 5/3$, while the ionospheric population follows a polytropic equation

185   varying smoothly between isobaric and adiabatic as $\gamma_{ion} = a(1 + (a/\gamma_{sw})^4)^{-1/4}$ where

186    $a = (\log(n_e))^{-1}$ and n_e is the ionospheric electron density.

187   To initialize the simulation, ion macroparticles are loaded to match ionspheric pro-

188   files computed assuming photo-equilibrium. For the first 2500 timesteps, planetary ion

189   motion is inhibited to allow a bow shock to develop before direct interaction of the so-

190   lar wind with the ionosphere. Additionally, this HELIOSARES run was simulated using

191   a different thermosphere, exoshere, and photoionization rates than are discussed in Sec-

192   tion 2.4. Full 3D models for the exosphere and thermosphere generated for solar median,

193   LS=90 using LMD-MGCM (Laboratoire de Méteorologie Dynamique Martian General

194   Circulation Model) [*González-Galindo et al.*, 2007] were utilized. Although they are not

195   identical to the models used for the rest of the simulations, they are similar when aver-

196   aged radially and should not greatly affect the presented results. The photoproduction is

197   based on the EUVAC (EUV model for Aeronomic Calculations) model [*Richards et al.*,

198   1994], which takes into account 27 wavelength groups, combine with the ionization and

199   absorption cross sections for each species from *Schunk and Nagy* [2000]. The computed

200   photoionization frequencies are similar, with less than 20% difference from the other mod-

201   els.

202   This RHybrid run uses a cartesian grid with a resolution of 113 km, bounds $X, Y, Z =$

203    $\pm 4 R_M$, and does not include crustal fields. Resistivity and electron velocity are set as zero

204   at the altitude of 300 km and below. All ions are absorbed and removed from the simu-

205   lation at the altitude of 200 km and below. Ionospheric O^+ and O_2^+ ions are emitted up-

206   wards from a spherical shell at 400 km with the temperature of 2×10^4 K. The emission

207   has a maximum flux at noon and cos(SZA) (Solar Zenith Angle) dependence towards ter-

208   minator where the flux reaches 10% of the noon value and is constant for the nightside.

209   Total ionospheric emission rates are $1.4 \times 10^{25} s^{-1}$ for O^+ and $2 \times 10^{25} s^{-1}$ for O_2^+. Photoion-

210   ization of the exospheric monatomic oxygen and hydrogen neutral coronas are included at

211   the altitude of 400 km and above in the dayside. The total photoionization rate in the sim-

212   ulation domain is $2.15 \times 10^{24} s^{-1}$ for hydrogen and $2.67 \times 10^{23} s^{-1}$ for monatomic oxygen.

213   The exospheric neutral profiles and ionospheric emission rates are the same as in earlier

214   studies such as *Brain et al.* [2010]; *Jarvinen et al.* [2016].

228 **Figure 2.** Slices in the XZ (*top*) and XY (*bottom*) planes. From top to bottom the rows show H^+ number

229 density, O^+ number density, and magnetic field magnitude. The columns indicate the model, from left to

230 right: BATSRUS-MS, BATSRUS-MF, BATSRUS-MF+Pe, RHybrid, HELIOSARES. The empty space in the

231 HELIOSARES data occurs because a slightly smaller domain is simulated while the plotting limits are kept

232 constant. Each column uses identical color space limits.

233 **Figure 3.** Flythrough of model results of the inbound and outbound portion of the orbit (#2349, 12/14/15)

234 excluding periapsis with corresponding *Maven* data. Panels show H^+ number density and magnetic field

235 magnitude. The location at which the orbit passes through the analytic boundary locations [*Trotignon et al.*,

236 2006] for the bow shock and MPB/IMB are plotted as vertical dashed lines.

2.4 Inner Boundary

216 For all models except HELIOSARES, a 3D neutral atmosphere and 1D exosphere

217 were used. The 3D neutral atmosphere was computed using the Mars Global Ionosphere-

218 Thermosphere Model (MGITM) [*Bougher et al.*, 2015] for for an areocentric longitude of

219 the Sun (LS) of 90 degrees at moderate EUV (F10.7=130). MGITM uses Martian physi-

220 cal parameters, ion-neutral chemistry, and radiative processes in order to simulate the dy-

221 namical structure of the Mars from the surface to the exosphere. The exosphere is imple-

222 mented via 1D profiles for hydrogen **[*Chaufray et al.*, 2008]** and oxygen [*Lee et al.*, 2015],

223 with oxygen containing both a hot and cold component. Photoionization rates were also

224 calculated using MGITM, and the additional rate coefficients were set from *Schunk and*

225 *Nagy* [2000].

3 Results

3.1 Boundaries

237 The interaction of the solar wind with the Martian plasma environment produces

238 several boundaries and transitions within the plasma, including the bow shock, and the

239 transition region including the Magnetic Pileup Boundary (MPB) due to the pileup of

240 the IMF as it drapes around the planet and the Induced Magnetosphere Boundary (IMB)

241 marked by a transition from solar wind to planetary plasma *Nagy et al.* [2004].

242   Fig. 2 shows slices of H^+, O^+, and magnetic field magnitude in the Y=0 and Z=0

243   planes for each model. Overplotted in white are the locations of the empirical bow shock

244   and MPB boundaries [*Trotignon et al.*, 2006].

245   Each model well predicts the magnetic standoff distance and the position of the bow

246   shock along the Mars-Sun line. Along the wings of the bow shock the H^+ and magnetic

247   field magnitude slices show that all the BATSRUS models show a more extended shock

248   region than the conic fits, while both hybrid models show a more compressed shock re-

249   gion. The shock boundary in the fluid models is symmetric with respect to Y and Z. This

250   general lack of asymmetry is driven by an almost entirely +y oriented IMF.

251   The HELIOSARES bow shock is more compressed in the $+\vec{z}$ hemisphere than the

252    $-\vec{z}$ hemisphere, driven by the electron pressure gradient and motional electric field, which

253   points inward in the $-\vec{z}$ hemisphere and outward in $+\vec{z}$ hemisphere. As described in *Simon*

254   *et al.* [2007], these two forces lead to the formation of a sharply pronounced boundary

255   layer in the hemisphere where they are antiparallel. This effect is present in simulations

256   that treat the ions kinetically, so is not present in the MHD models. RHybrid also shows

257   asymmetry due to the motional electric field, but it is less pronounced in the $y = 0$ plane

258   compared to HELIOSARES.

259   The transition to planetary plasma (depicted by O^+) along the subsolar line occurs

260   simultaneously with the empirical boundary location for all models. In the X-Z plane (2a),

261   the BATSRUS-MS and BATSRUS-Pe models show little asymmetry in O^+ number den-

262   sity and well reproduce the empirical boundary location, while BATSRUS-MF and HE-

263   LIOSARES show strong Z asymmetry, and RHybrid only shows planetary plasma along

264   the plume and current sheet outside the ionosphere. All models show very little asymme-

265   try in the X-Y plane (2b).

266   Fig. 3 confirms the intuition gained with slices, but by flying through the models

267   we are also able to compare with *Maven* data from this orbit. On the inbound portion of

268   the orbit the *Maven* data show a bow shock at roughly the same location as the empirical

269   boundary, but the outbound crossing happens lower in altitude than the empirical crossing.

270   This indicates the presence of some some combination of asymmetry and time variabil-

271   ity. As the shocked region is relatively extended in the MHD models, none of them show

272   a bow shock crossing in this flythrough, instead *Maven*'s orbit encounters only modeled

273   magnetosheath and lower. Thus, both the H^+ number density and the magnetic field mag-

Figure 4. Flythrough of model results at low altitudes with corresponding *Maven* data from orbit #2349 (12/14/15). Panels show O_2^+, O^+, CO_2^+ number densities from top to bottom. RHybrid results are excluded due to the lack of ionosphere. No HELIOSARES results are shown for CO_2^+ because it was not included in the model.

nitude appear to be larger in the fluid models than the data and hybrid models. The RHybrid and HELIOSARES models both show a clear shock crossing that is lower in altitude than the inbound *Maven* crossing, but very similar on the outbound crossing.

3.2 Low Altitude

Maven enters the ionosphere on Mars' northern hemisphere along the the terminator plane. Measurements in this region from the Neutral Gas and Ion Mass Spectrometer (NGIMS) [*Mahaffy et al.*, 2015] are shown along with model results in Fig. 4. RHybrid is not shown here due to the absence of ionosphere in the run.

At the lowest altitudes there is strong agreement across all models and data for O^+, O_2^+, and CO_2^+, indicating that the ion production physics is well represented in each model. Previous studies, including *Ma et al.* [2015] also found good agreement in ionospheric densities between data and models. The difference in shapes of the heavy ion profiles are indictative of different dominant heights. The relative steepness in decline with altitude between ions is and shape of the distributions are consistent with predicted scale heights. The jaggedness of the HELIOSARES profiles is due to the limited resolution of the grid that the ion macroparticles are deposited onto. The shallow drop off of the HELIOSARES densities on the outbound segment relative to the inbound segment is due to contributions from the southern hemisphere slow escaping ions (see Section 3.3).

For each ion, the inbound portion of the *Maven* data shows some excess number density relative to the to steep drop off shown by the models, likely due to time and spatial variability not captured by the models.

3.3 Southern Hemisphere

Cold ion escape likely plays an important role in heavy ion loss on Mars [*Fränz et al.*, 2015; *Dong et al.*, 2015b]. Here we discuss differences betwen the models in the

305 **Figure 5.** Slices of O^+ number density with magnetic field vectors overlaid. Panels show (top to bot-

306 tom) planes $Z = -1.3R_M, Y = 0, X = 0$, and (left to right) simulations BATSRUS-MS, BATSRUS-MF,

307 BATSRUS-MF+Pe, RHybrid, and HELIOSARES. All colorbars are consistent and labeled to the right.

302 southern (-z) hemisphere where an extended population of cold ions connects to the tail.

303 This region of the tail is not affected by the northern pickup ions, which we will discuss

304 in a future paper.

308 As shown in Fig. 5, all models show a region of planetary ions that extends from

309 the southern hemisphere towards the tail. These ions are cold and have near zero bulk

310 velocity. HELIOSARES shows slightly higher number densities than the BATSRUS and

311 RHybrid models and the region extends farther in the -z direction.

312 Fig. 5 also shows vectors of the magnetic field. From this figure it is clear that the

313 topology varies substantially in this region across the models. The top panel shows a

314 draped field configuration in the BATSRUS and RHybrid models, while the field in the

315 HELIOSARES model appears toroidal where the ion densities are highest. In the YZ

316 plane (*middle panels*) the HELIOSARES model again appears toroidal in the tail, while

317 the BATSRUS models all show magnetic field vectors predominately in the $\pm x$ direction.

318 From examining the field line topology in three dimensions the magnetic field in

319 HELIOSARES appears coiled in the southern hemisphere, forming a channel for slow ion

320 escape. This differs from the magnetic topology in BATSRUS which appears more like a

321 basic current sheet model created by a draped IMF. These differences are likely related to

322 differences in the obstacle boundary and conductivity.

3.4 Global Escape

324 One of the foremost areas of interest to the Martian community is the rate at which

325 ions are lost to space, and the channels this escape procedes through. Global ion escape

326 has been measured [*Lundin et al.*, 1989; *Barabash et al.*, 2007], as has variance in escape

327 with solar wind and EUV [*Ramstad et al.*, 2015], and variance with crustal fields [*Ram-*

328 *stad et al.*, 2016]; for full review of global ion escape at Mars see *Dubinin et al.* [2011].

329 *Brain et al.* [2015] has mapped the spatial distribution of inflowing and outflowing ion

fluxes by averaging data across many orbits. Here we present similar maps to *Brain et al.* [2015] but of the entire system at a single instance in time as simulated by the models.

Fig. 6 shows maps of the modelled ion fluxes at $1.8R_M$ across latitude and longitude in the Mars-Solar-Electric field (MSE) coordinate system; $+\vec{x}$ is the direction from Mars to the sun, $+\vec{z}$ is along the upstream solar wind motional electric field, and $+\vec{y}$ is the completion of a right-handed coordinate system. The maps are created by defining a set of points in a spherical shell, equally spaced in five degree increments in latitude and longitude, and probing the net ion flux at each point in each model without averaging or interpolation.

On the dayside (centered on longitude = 0), all models have inbound heavy ion flux. In BATSRUS-MS this is symmetrical around latitude = 0 and longitude = 0. In the BATSRUS-MF, BATSRUS-MF+Pe, RHybrid, and HELIOSARES models the dayside inbound ion flux is confined to the southern hemisphere.

This symmetry breaking is related to the plume presence in the BATSRUS-MF, BATSRUS-MF+Pe, RHybrid, and HELIOSARES models. The plume feature is seen as a dark blue (outbound flux) feature at high latitudes ($> 45°$ directly above the northern pole) centered around longitude $−30°$, and as a channel connecting to the tailward outbound flux centered at longitude $180°$. Furthermore, due to the limited number of heavy ions at large radii on the dayside, the H^+ dynamics dictate the ion flux for BATSRUS-MS.

All models except HELIOSARES show predominately outbound flux in the tail. RHybrid shows only outbound flux, while all the BATSRUS models have regions where ions are inflowing. These inflow regions are present in the same locations at lower altitudes (down to $1.1R_M$) but shrink at higher altitudes out to $\sim 3.0R_M$). They are also correlated to the magnetic field vector at this point. This indicates that they are likely related to the dynamics of the current sheet and the presence of crustal fields, as only RHybrid does not include crustal fields. As the the dynamics of these regions are sensitive to tail plasma proccesses, crustal field implementation, and low altitude nightside ions, and our orbit does not probe this region, we leave further study to future work.

We find that the modelled maps are qualitatively similar to maps created from *Maven* data [*Brain et al.*, 2015]. The dayside shows predominately inward flux, while the tail shows outward flux. Northern MSE latitude shows relatively more outward flux than the

Figure 6. Total heavy ion flux maps for (Left to right, top to bottom) BATSRUS-MS, RHybrid, BATSRUS-MF+Pe, BATSRUS-MF+Pe, HELIOSARES, *Maven* data. Axes limits and colorbar are identical for each panel (except the *Maven* panel which is labeled separately), with blue indicating outward flux and red indicating inward flux. The map created from *Maven* data is adopted from [*Brain et al.*, 2015].

southern MSE latitude region. However, coverage of this space is still relatively incomplete due to the limited amount of *Maven* orbits there have been, so further conclusions and more detailed model-data comparison are not yet possible.

By summing across all latitude/longitude bins and weighting by area, global ion fluxes can be calculated for a given radius for each model. The rates for $R = 1.8R_M$ are shown in Table 3, along with observed rates calculated by *Brain et al.* [2015] and [*Ramstad et al.*, 2015]. A full comparison with all observed rates is beyond the scope of this paper, we just show *Brain et al.* [2015] for comparison with the escape maps and [*Ramstad et al.*, 2015] for a recent result calculated for comparable solar wind conditions. For a full comparison of ion escape rates at Mars, see *Dubinin et al.* [2011].

These results are very constant with radius for all models and are very similar for such a large variation in escape maps. There is greater agreement between these rates than those calculated by *Brain et al.* [2010], indicating some level of convergence over time across models. These rates are also within a factor of three of those calculated by *Brain et al.* [2015], though those rates are for a wide variety of solar wind conditions and planetary orientation, and also include all heavy ion species. When compared to rates calculated by *Ramstad et al.* [2015] for similar solar wind and EUV conditions our calculated rates are all within the appropriate range ($2.1 \pm 1.1 \times 10^{24} s^{-1}$).

4 Conclusion

Five models of the Martian magnetosphere have been run for nearly identical input conditions (aside from the small variations discussed in Section 2); these models were then compared to each other and to *Maven* data. The input conditions were chosen to reflect the upstream drivers of *Maven* orbit #2349, an orbit chosen because the solar wind data is steady and typical, while the rest of the orbit probes other interesting regions. Model flythroughs along the orbit trajectory, slices through different regions, spherical ion flux maps, and global escape rates were obtained for each dataset.

Table 3. Calculated and observed escape rates for O^+, O_2^+, and total. For each model the total includes all species included in the model, while the total for the observed rates includes all ions with energies above the relevant cutoff.

Model/Survey	O^+ ($\times 10^{24}$ #/s)	O_2^+ ($\times 10^{24}$ #/s)	Total ($\times 10^{24}$ #/s)
BATSRUS-MS	1.0	1.1	2.1
BATSRUS-MF	0.6	1.8	2.4
BATSRUS-MF+Pe	1.3	2.1	3.4
RHybrid	1.1	1.1	2.2
HELIOSARES	2.3	0.9	3.2
Brain et al. [2015]	-	-	1.6
Ramstad et al. [2015]	-	-	2.1 ± 1.1

Most models showed little boundary asymmetry due to the IMF being nearly completely in the $+\vec{y}$ direction. The overall extent of the shocked region was larger in the fluid models than both the empirical boundaries and the *Maven* results, while the hybrid models matched the outbound crossing very well.

From comparing NGIMS ion data to model flythroughs at low altitude it is clear that all models that have an inner boundary lower than ~ 200 km do a good job modelling the low altitude day-side ions. Both overall normalization and scale heights are well recreated by all the BATSRUS models as well as HELIOSARES.

The outflow of cold ions in the southern hemisphere varied substantially across models. More study of the effects of lower boundary conditions and the impact they have on the magnetic topology and ion outflow in tail could impact ion escape estimates. However, although this outflow was much denser and more localized in the HELIOSARES model than the BATSRUS models, overall global escape rates were relatively constant.

Future efforts on this front are still necessary. This model challenge focused specifically on one orbit with a moderate solar wind and +y directed IMF. Changing input conditions will vary how the solar wind interacts with the ionosphere and likely how variations in model physics appear. Furthermore, we have limited our analysis to certain regions, and delayed comparison of the plume region for a future paper. More analysis and com-

parisons with data from additional *Maven* orbits will be necessary to probe other regions such as the tail.

5 Acknowledgments

References

Arkani-Hamed, J. (2001), A 50-degree spherical harmonic model of the magnetic field of Mars, J. Geophys. Res., *106*, 23,197–23,208, doi:10.1029/2000JE001365.

Barabash, S., A. Fedorov, R. Lundin, and J.-A. Sauvaud (2007), Martian Atmospheric Erosion Rates, *Science*, *315*, 501, doi:10.1126/science.1134358.

Bertucci, C., C. Mazelle, M. Acuña, C. Russell, and J. Slavin (2005), Structure of the magnetic pileup boundary at mars and venus, *J Geophys Res Space Phys 1978 2012*, *110*(A1), doi:10.1029/2004JA010592.

Boesswetter, A., H. Lammer, Y. Kulikov, U. Motschmann, and S. Simon (2010), Non-thermal water loss of the early Mars: 3D multi-ion hybrid simulations, Planet. Space Sci., *58*, 2031–2043, doi:10.1016/j.pss.2010.10.003.

Bößwetter, A., T. Bagdonat, U. Motschmann, and K. Sauer (2004), Plasma boundaries at Mars: a 3-D simulation study, *Annales Geophysicae*, *22*, 4363–4379, doi: 10.5194/angeo-22-4363-2004.

Bougher, S. W., D. Pawlowski, J. M. Bell, S. Nelli, T. McDunn, J. R. Murphy, M. Chizek, and A. Ridley (2015), Mars Global Ionosphere-Thermosphere Model: Solar cycle, seasonal, and diurnal variations of the Mars upper atmosphere, *Journal of Geophysical Research (Planets)*, *120*, 311–342, doi:10.1002/2014JE004715.

Brain, D., S. Barabash, A. Boesswetter, S. Bougher, S. Brecht, G. Chanteur, D. Hurley, E. Dubinin, X. Fang, M. Fraenz, J. Halekas, E. Harnett, M. Holmstrom, E. Kallio, H. Lammer, S. Ledvina, M. Liemohn, K. Liu, J. Luhmann, Y. Ma, R. Modolo, A. Nagy, U. Motschmann, H. Nilsson, H. Shinagawa, S. Simon, and N. Terada (2010), A comparison of global models for the solar wind interaction with Mars, Icarus, *206*, 139–151, doi:10.1016/j.icarus.2009.06.030.

Brain, D., M. JP, J. Halekas, J. Connerney, S. Bougher, S. Curry, C. Dong, Y. Dong, F. Eparvier, X. Fang, K. Fortier, T. Hara, Y. Harada, B. Jakosky, R. Lillis, R. Livi, J. Luhmann, Y. Ma, R. Modolo, and K. Seki (2015), The spatial distribution of planetary ion fluxes near mars observed by MAVEN, Geophys. Res. Lett., *42*(21), 9142–9148, doi:10.1002/2015GL065293.

Brecht, S. H., and S. A. Ledvina (2014), The role of the Martian crustal magnetic fields in controlling ionospheric loss, Geophys. Res. Lett., *41*, 5340–5346, doi: 10.1002/2014GL060841.

Brecht, S. H., S. A. Ledvina, and S. W. Bougher (2016), Ionospheric loss from mars as predicted by hybrid particle simulations, *Journal of Geophysical Research: Space Physics*, *121*(10), 10,190–10,208, doi:10.1002/2016JA022548, 2016JA022548.

Cain, J. C., B. B. Ferguson, and D. Mozzoni (2003), An n = 90 internal potential function of the Martian crustal magnetic field, *Journal of Geophysical Research (Planets)*, *108*, 5008, doi:10.1029/2000JE001487.

Chanteur, G. M., E. Dubinin, R. Modolo, and M. Fraenz (2009), Capture of solar wind alpha-particles by the martian atmosphere, *Geophysical Research Letters*, *36*(23), n/a– n/a, doi:10.1029/2009GL040235, l23105.

Chaufray, J. Y., J. L. Bertaux, F. Leblanc, and E. Quémerais (2008), Observation of the hydrogen corona with SPICAM on Mars Express, Icarus, *195*, 598–613, doi: 10.1016/j.icarus.2008.01.009.

Connerney, J. E. P., J. Espley, P. Lawton, S. Murphy, J. Odom, R. Oliversen, and D. Sheppard (2015), The MAVEN Magnetic Field Investigation, Space Sci. Rev., *195*, 257–291, doi:10.1007/s11214-015-0169-4.

Cravens, T. E., A. Hoppe, S. A. Ledvina, and S. McKenna-Lawlor (2002), Pickup ions near mars associated with escaping oxygen atoms, *Journal of Geophysical Research: Space Physics*, *107*(A8), SMP 7–1–SMP 7–10, doi:10.1029/2001JA000125.

Dong, C., S. W. Bougher, Y. Ma, G. Toth, Y. Lee, A. F. Nagy, V. Tenishev, D. J. Pawlowski, M. R. Combi, and D. Najib (2015), Solar wind interaction with the martian upper atmosphere: Crustal field orientation, solar cycle, and seasonal variations, *Journal of Geophysical Research: Space Physics*, *120*(9), 7857–7872, doi: 10.1002/2015JA020990, 2015JA020990.

Dong, C., Y. Ma, S. W. Bougher, G. Toth, A. F. Nagy, J. S. Halekas, Y. Dong, S. M. Curry, J. G. Luhmann, D. Brain, J. E. P. Connerney, J. Espley, P. Mahaffy, M. Benna, J. P. McFadden, D. L. Mitchell, G. A. DiBraccio, R. J. Lillis, B. M. Jakosky, and J. M. Grebowsky (2015a), Multifluid MHD study of the solar wind interaction with Mars' upper atmosphere during the 2015 March 8th ICME event, Geophys. Res. Lett., *42*, 9103–9112, doi:10.1002/2015GL065944.

Dong, Y., X. Fang, D. A. Brain, J. P. McFadden, J. S. Halekas, J. E. Connerney, S. M. Curry, Y. Harada, J. G. Luhmann, and B. M. Jakosky (2015b), Strong plume fluxes at Mars observed by MAVEN: An important planetary ion escape channel, Geophys. Res. Lett., *42*, 8942–8950, doi:10.1002/2015GL065346.

Dryer, M., and G. Heckman (1967), On the hypersonic analogue as applied to planetary interaction with the solar plasma, Planet. Space Sci..

Dubinin, E., M. Fraenz, A. Fedorov, R. Lundin, N. Edberg, F. Duru, and O. Vaisberg (2011), Ion Energization and Escape on Mars and Venus, Space Sci. Rev., *162*, 173–211, doi:10.1007/s11214-011-9831-7.

Fang, X., M. W. Liemohn, A. F. Nagy, Y. Ma, D. L. De Zeeuw, J. U. Kozyra, and T. H. Zurbuchen (2008), Pickup oxygen ion velocity space and spatial distribution around mars, *Journal of Geophysical Research: Space Physics*, *113*(A2), n/a–n/a, doi: 10.1029/2007JA012736, a02210.

Fang, X., M. W. Liemohn, A. F. Nagy, J. G. Luhmann, and Y. Ma (2010), On the effect of the martian crustal magnetic field on atmospheric erosion, pp. 130–138, doi: 10.1016/j.icarus.2009.01.012.

Fang, X., Y. Ma, D. Brain, Y. Dong, and R. Lillis (2015), Control of Mars global atmospheric loss by the continuous rotation of the crustal magnetic field: A time-dependent MHD study, *Journal of Geophysical Research (Space Physics)*, *120*, 10, doi: 10.1002/2015JA021605.

Fränz, M., E. Dubinin, D. Andrews, S. Barabash, H. Nilsson, and A. Fedorov (2015), Cold ion escape from the Martian ionosphere, Planet. Space Sci., *119*, 92–102, doi:

508   10.1016/j.pss.2015.07.012.

509   Glocer, A., G. Tóth, Y. Ma, T. Gombosi, J.-C. Zhang, and L. M. Kistler (2009), Multifluid

510   Block-Adaptive-Tree Solar wind Roe-type Upwind Scheme: Magnetospheric composi-

511   tion and dynamics during geomagnetic storms: Initial results, *Journal of Geophysical*

512   *Research (Space Physics)*, *114*, A12203, doi:10.1029/2009JA014418.

513   González-Galindo, F., F. Forget, M. A. López-Valverde, M. Angelats I Coll, and S. W.

514   Bougher (2007), LMD-MGCM: The First Ground-to-Exosphere General Circulation

515   Model of the Martian Atmosphere, in *Seventh International Conference on Mars*, *LPI*

516   *Contributions*, vol. 1353, p. 3099.

517   Gunell, H., M. Holmström, E. Kallio, P. Janhunen, and K. Dennerl (2004), X rays from

518   solar wind charge exchange at mars: A comparison of simulations and observations,

519   *Geophysical Research Letters*, *31*(22), n/a–n/a, doi:10.1029/2004GL020953, l22801.

520   Gunell, H., M. Holmström, S. Barabash, E. Kallio, P. Janhunen, A. F. Nagy, and Y. Ma

521   (2006), Planetary ENA imaging: Effects of different interaction models for Mars,

522   Planet. Space Sci., *54*, 117–131, doi:10.1016/j.pss.2005.04.002.

523   Halekas, J. S., E. R. Taylor, G. Dalton, G. Johnson, D. W. Curtis, J. P. McFadden, D. L.

524   Mitchell, R. P. Lin, and B. M. Jakosky (2015), The Solar Wind Ion Analyzer for

525   MAVEN, Space Sci. Rev., *195*, 125–151, doi:10.1007/s11214-013-0029-z.

526   Harnett, E. M., and R. M. Winglee (2007), High-resolution multifluid simulations of the

527   plasma environment near the martian magnetic anomalies, *Journal of Geophysical Re-*

528   *search: Space Physics*, *112*(A5), n/a–n/a, doi:10.1029/2006JA012001, a05207.

529   Holmstrom, M., and X.-D. Wang (2015), Mars as a comet: Solar wind in-

530   teraction on a large scale, *Planetary and Space Science*, *119*, 43 – 47, doi:

531   https://doi.org/10.1016/j.pss.2015.09.017.

532   Hurrell, J. W. (1995), Comparison of ncar community climate model (ccm) climates, *Cli-*

533   *mate Dynamics*, *11*(1), 25–50, doi:10.1007/BF00220675.

534   Jakosky, B. M., R. P. Lin, J. M. Grebowsky, J. G. Luhmann, D. F. Mitchell, G. Beu-

535   telschies, T. Priser, M. Acuna, L. Andersson, D. Baird, D. Baker, R. Bartlett, M. Benna,

536   S. Bougher, D. Brain, D. Carson, S. Cauffman, P. Chamberlin, J.-Y. Chaufray,

537   O. Cheatom, J. Clarke, J. Connerney, T. Cravens, D. Curtis, G. Delory, S. Demcak,

538   A. DeWolfe, F. Eparvier, R. Ergun, A. Eriksson, J. Espley, X. Fang, D. Folta, J. Fox,

539   C. Gomez-Rosa, S. Habenicht, J. Halekas, G. Holsclaw, M. Houghton, R. Howard,

540   M. Jarosz, N. Jedrich, M. Johnson, W. Kasprzak, M. Kelley, T. King, M. Lankton,

D. Larson, F. Leblanc, F. Lefevre, R. Lillis, P. Mahaffy, C. Mazelle, W. McClintock, J. McFadden, D. L. Mitchell, F. Montmessin, J. Morrissey, W. Peterson, W. Possel, J.-A. Sauvaud, N. Schneider, W. Sidney, S. Sparacino, A. I. F. Stewart, R. Tolson, D. Toublanc, C. Waters, T. Woods, R. Yelle, and R. Zurek (2015), The Mars Atmosphere and Volatile Evolution (MAVEN) Mission, *Space Science Reviews*, *195*, 3–48, doi: 10.1007/s11214-015-0139-x.

Jarvinen, R., D. A. Brain, and J. G. Luhmann (2016), Dynamics of planetary ions in the induced magnetospheres of Venus and Mars, Planet. Space Sci., *127*, 1–14, doi: 10.1016/j.pss.2015.08.012.

Jarvinen, R., D. Brain, R. Modolo, A. Fedorov, HolmstrÃűm, and M. (2018), Oxygen Ion Energization at Mars: Comparison of MAVEN and Mars Express Observations to Global Hybrid Simulation, *Journal of Geophysical Research: Space Physics*, doi: doi:10.1002/2017JA024884.

Kallio, E., and P. Janhunen (2002), Ion escape from mars in a quasiâĂŘneutral hybrid model, pp. SIA 1–1–SIA 1–21, doi:10.1029/2001JA000090.

Kallio, E., A. Fedorov, E. Budnik, T. Säles, P. Janhunen, W. Schmidt, H. Koskinen, P. Riihelä, S. Barabash, R. Lundin, M. Holmström, H. Gunell, K. Brinkfeldt, Y. Futaana, H. Andersson, M. Yamauchi, A. Grigoriev, J. Sauvaud, J. Thocaven, J. Winningham, R. Frahm, J. Sharber, J. Scherrer, A. Coates, D. Linder, D. Kataria, J. Kozyra, J. Luhmann, E. Roelof, D. Williams, S. Livi, C. Curtis, K. Hsieh, B. Sandel, M. Grande, M. Carter, M. S., S. Orsini, C. R., M. Maggi, P. Wurz, P. Bochsler, N. Krupp, J. Woch, M. Fränz, K. Asamura, and C. Dierker (2006a), Ion escape at mars: Comparison of a 3-D hybrid simulation with mars express IMA/ASPERA-3 measurements, *Icarus*, *182*(2), 350–359, doi:10.1016/j.icarus.2005.09.018.

Kallio, E., S. Barabash, K. Brinkfeldt, H. Gunell, M. Holmström, Y. Futaana, W. Schmidt, T. Säles, H. Koskinen, P. Riihelä, R. Lundin, H. Andersson, M. Yamauchi, A. Grigoriev, J. Winningham, R. Frahm, J. Sharber, J. Scherrer, A. Coates, D. Linder, D. Kataria, J. Kozyra, J. Luhmann, E. Roelof, D. Williams, S. Livi, P. Brandt, C. Curtis, K. Hsieh, B. Sandel, M. Grande, M. Carter, J. Sauvaud, A. Fedorov, J. Thocaven, M. S., S. Orsini, C. R., M. Maggi, P. Wurz, P. Bochsler, N. Krupp, J. Woch, M. Fränz, K. Asamura, and C. Dierker (2006b), Energetic neutral atoms (ENA) at mars: Properties of the hydrogen atoms produced upstream of the martian bow shock and implications for ENA sounding technique around non-magnetized planets, *Icarus*, *182*(2),

574   448–463, doi:10.1016/j.icarus.2005.12.019.

575   Kim, J.-h., O. Agertz, R. Teyssier, M. J. Butler, D. Ceverino, J.-H. Choi, R. Feldmann,

576   B. W. Keller, A. Lupi, T. Quinn, Y. Revaz, S. Wallace, N. Y. Gnedin, S. N. Leitner,

577   S. Shen, B. D. Smith, R. Thompson, M. J. Turk, T. Abel, K. S. Arraki, S. M. Benin-

578   casa, S. Chakrabarti, C. DeGraf, A. Dekel, N. J. Goldbaum, P. F. Hopkins, C. B. Hum-

579   mels, A. Klypin, H. Li, P. Madau, N. Mandelker, L. Mayer, K. Nagamine, S. Nickerson,

580   B. W. O'Shea, J. R. Primack, S. Roca-Fàbrega, V. Semenov, I. Shimizu, C. M. Simp-

581   son, K. Todoroki, J. W. Wadsley, J. H. Wise, and AGORA Collaboration (2016), The

582   AGORA High-resolution Galaxy Simulations Comparison Project. II. Isolated Disk Test,

583   ApJ, *833*, 202, doi:10.3847/1538-4357/833/2/202.

584   Ledvina, S., Y. Ma, and E. Kallio (2008), Modeling and simulating flowing plasmas and

585   related phenomena, *Space Sci Rev*, *139*(1-4), 143–189, doi:10.1007/s11214-008-9384-6.

586   Lee, Y., M. R. Combi, V. Tenishev, S. W. Bougher, and R. J. Lillis (2015), Hot oxygen

587   corona at Mars and the photochemical escape of oxygen: Improved description of the

588   thermosphere, ionosphere, and exosphere, *Journal of Geophysical Research (Planets)*,

589   *120*, 1880–1892, doi:10.1002/2015JE004890.

590   Liemohn, M. W., Y. Ma, R. A. Frahm, X. Fang, J. U. Kozyra, A. F. Nagy, J. D. Winning-

591   ham, J. R. Sharber, S. Barabash, and R. Lundin (2006), Mars Global MHD Predictions

592   of Magnetic Connectivity Between the Dayside Ionosphere and the Magnetospheric

593   Flanks, Space Sci. Rev., *126*, 63–76, doi:10.1007/s11214-006-9116-8.

594   Liemohn, M. W., S. M. Curry, X. Fang, and Y. Ma (2013), Comparison of high-altitude

595   production and ionospheric outflow contributions to O^+ loss at Mars, *Journal of Geo-*

596   *physical Research (Space Physics)*, *118*, 4093–4107, doi:10.1002/jgra.50388.

597   Lundin, R., A. Zakharov, R. Pellinen, H. Borg, B. Hultqvist, N. Pissarenko, E. M. Du-

598   binin, S. W. Barabash, I. Liede, and H. Koskinen (1989), First measurements of the

599   ionospheric plasma escape from Mars, Nature, *341*, 609–612, doi:10.1038/341609a0.

600   Ma, Y., A. F. Nagy, I. V. Sokolov, and K. C. Hansen (2004), Three-dimensional, mul-

601   tispecies, high spatial resolution mhd studies of the solar wind interaction with

602   mars, *Journal of Geophysical Research: Space Physics*, *109*(A7), n/a–n/a, doi:

603   10.1029/2003JA010367, a07211.

604   Ma, Y., C. T. Russell, A. F. Nagy, G. Toth, C. Dong, and S. W. Bougher (2013), Multi-

605   fluid MHD Study of the Solar Wind Induced Plasma Escape from the Martian Atmo-

606   sphere, *AGU Fall Meeting Abstracts*.

Author Manuscript

21

Ma, Y., X. Fang, C. T. Russell, A. F. Nagy, G. Toth, J. G. Luhmann, D. A. Brain, and C. Dong (2014), Effects of crustal field rotation on the solar wind plasma interaction with mars, *Geophysical Research Letters*, *41*(19), 6563–6569, doi: 10.1002/2014GL060785, 2014GL060785.

Ma, Y., C. Russell, X. Fang, and Y. Dong (2015), MHD model results of solar wind interaction with mars and comparison with MAVEN plasma observations, *Geophysical âĂę*, doi:10.1002/2015GL065218.

Ma, Y. J., C. T. Russell, A. F. Nagy, G. Toth, M. K. Dougherty, A. Wellbrock, A. J. Coates, P. Garnier, J.-E. Wahlund, T. E. Cravens, M. S. Richard, and F. J. Crary (2011), The importance of thermal electron heating in titan's ionosphere: Comparison with cassini t34 flyby, *Journal of Geophysical Research: Space Physics*, *116*(A10), n/a–n/a, doi:10.1029/2011JA016657, a10213.

Ma, Y. J., C. T. Russell, X. Fang, C. F. Dong, A. F. Nagy, G. Toth, J. S. Halekas, J. E. P. Connerney, J. R. Espley, P. R. Mahaffy, M. Benna, J. McFadden, D. L. Mitchell, L. Andersson, and B. M. Jakosky (2017), Variations of the martian plasma environment during the icme passage on 8 march 2015: A time-dependent mhd study, *Journal of Geophysical Research: Space Physics*, *122*(2), 1714–1730, doi:10.1002/2016JA023402, 2016JA023402.

Mahaffy, P. R., M. Benna, T. King, D. N. Harpold, R. Arvey, M. Barciniak, M. Bendt, D. Carrigan, T. Errigo, V. Holmes, C. S. Johnson, J. Kellogg, P. Kimvilakani, M. Lefavor, J. Hengemihle, F. Jaeger, E. Lyness, J. Maurer, A. Melak, F. Noreiga, M. Noriega, K. Patel, B. Prats, E. Raaen, F. Tan, E. Weidner, C. Gundersen, S. Battel, B. P. Block, K. Arnett, R. Miller, C. Cooper, C. Edmonson, and J. T. Nolan (2015), The Neutral Gas and Ion Mass Spectrometer on the Mars Atmosphere and Volatile Evolution Mission, Space Sci. Rev., *195*, 49–73, doi:10.1007/s11214-014-0091-1.

McFadden, J. P., O. Kortmann, D. Curtis, G. Dalton, G. Johnson, R. Abiad, R. Sterling, K. Hatch, P. Berg, C. Tiu, D. Gordon, S. Heavner, M. Robinson, M. Marckwordt, R. Lin, and B. Jakosky (2015), MAVEN SupraThermal and Thermal Ion Compostion (STATIC) Instrument, Space Sci. Rev., *195*, 199–256, doi:10.1007/s11214-015-0175-6.

Mitchell, D. L., C. Mazelle, J.-A. Sauvaud, J.-J. Thocaven, J. Rouzaud, A. Fedorov, P. Rouger, D. Toublanc, E. Taylor, D. Gordon, M. Robinson, S. Heavner, P. Turin, M. Diaz-Aguado, D. W. Curtis, R. P. Lin, and B. M. Jakosky (2016), The MAVEN Solar Wind Electron Analyzer, Space Sci. Rev., *200*, 495–528, doi:10.1007/s11214-015-

0232-1.

Modolo, R., G. M. Chanteur, E. Dubinin, and A. P. Matthews (2005), Influence of the solar EUV flux on the Martian plasma environment, *Annales Geophysicae*, *23*, 433–444, doi:10.5194/angeo-23-433-2005.

Modolo, R., G. M. Chanteur, E. Dubinin, and A. P. Matthews (2006), Simulated solar wind plasma interaction with the martian exosphere: influence of the solar euv flux on the bow shock and the magnetic pile-up boundary, *Annales Geophysicae*, *24*(12), 3403–3410, doi:10.5194/angeo-24-3403-2006.

Modolo, R., S. Hess, M. Mancini, F. Leblanc, J.-Y. Chaufray, D. Brain, L. Leclercq, R. Esteban-Hernãndez, G. Chanteur, P. Weill, F. Gonzãlez-Galindo, F. Forget, M. Yagi, and C. Mazelle (2016), Mars-solar wind interaction: Lathys, an improved parallel 3-d multispecies hybrid model, *Journal of Geophysical Research: Space Physics*, *121*(7), 6378–6399, doi:10.1002/2015JA022324, 2015JA022324.

Nagy, A. F., D. Winterhalter, K. Sauer, T. E. Cravens, S. Brecht, C. Mazelle, D. Crider, E. Kallio, A. Zakharov, E. Dubinin, M. Verigin, G. Kotova, W. I. Axford, C. Bertucci, and J. G. Trotignon (2004), The plasma Environment of Mars, *Space Science Reviews*, *111*, 33–114, doi:10.1023/B:SPAC.0000032718.47512.92.

Najib, D., A. F. Nagy, G. Tãşth, and Y. Ma (2011), Three-dimensional, multifluid, high spatial resolution mhd model studies of the solar wind interaction with mars, *Journal of Geophysical Research: Space Physics*, *116*(A5), n/a–n/a, doi:10.1029/2010JA016272, a05204.

Ramstad, R., S. Barabash, Y. Futaana, H. Nilsson, X.-D. Wang, and M. Holmström (2015), The Martian atmospheric ion escape rate dependence on solar wind and solar EUV conditions: 1. Seven years of Mars Express observations, *Journal of Geophysical Research (Planets)*, *120*, 1298–1309, doi:10.1002/2015JE004816.

Ramstad, R., S. Barabash, Y. Futaana, H. Nilsson, and M. Holmström (2016), Effects of the crustal magnetic fields on the Martian atmospheric ion escape rate, Geophys. Res. Lett., *43*, 10, doi:10.1002/2016GL070135.

Richards, P. G., J. A. Fennelly, and D. G. Torr (1994), Euvac: A solar euv flux model for aeronomic calculations, *Journal of Geophysical Research: Space Physics*, *99*(A5), 8981–8992, doi:10.1029/94JA00518.

Schunk, R., and A. Nagy (2000), *Ionospheres: Physics, Plasma Physics, and Chemistry*, Cambridge Atmospheric and Space Science Series, Cambridge University Press.

Simon, S., A. Boesswetter, T. Bagdonat, and U. Motschmann (2007), Physics of the Ion Composition Boundary: a comparative 3-D hybrid simulation study of Mars and Titan, *Annales Geophysicae*, *25*, 99–115, doi:10.5194/angeo-25-99-2007.

Spreiter, J., A. Summers, and A. Rizzi (1970), Solar wind flow past nonmagnetic planetsâĂŤVenus and mars, Planet. Space Sci..

Terada, N., H. Shinagawa, T. Tanaka, K. Murawski, and K. Terada (2009), A three-dimensional, multispecies, comprehensive mhd model of the solar wind interaction with the planet venus, *Journal of Geophysical Research: Space Physics*, *114*(A9), n/a–n/a, doi:10.1029/2008JA013937, a09208.

Trotignon, J. G., C. Mazelle, C. Bertucci, and M. H. Acuña (2006), Martian shock and magnetic pile-up boundary positions and shapes determined from the Phobos 2 and Mars Global Surveyor data sets, Planet. Space Sci., *54*, 357–369, doi: 10.1016/j.pss.2006.01.003.

Wang, X.-D., S. Barabash, Y. Futaana, A. Grigoriev, and P. Wurz (2014), Influence of Martian crustal magnetic anomalies on the emission of energetic neutral hydrogen atoms, *Journal of Geophysical Research (Space Physics)*, *119*, 8600–8609, doi: 10.1002/2014JA020307.

Wang, X.-D., M. Alho, R. Jarvinen, E. Kallio, S. Barabash, and Y. Futaana (2016), Emission of hydrogen energetic neutral atoms from the Martian subsolar magnetosheath, *Journal of Geophysical Research (Space Physics)*, *121*, 190–204, doi: 10.1002/2015JA021653.

Figure 1.
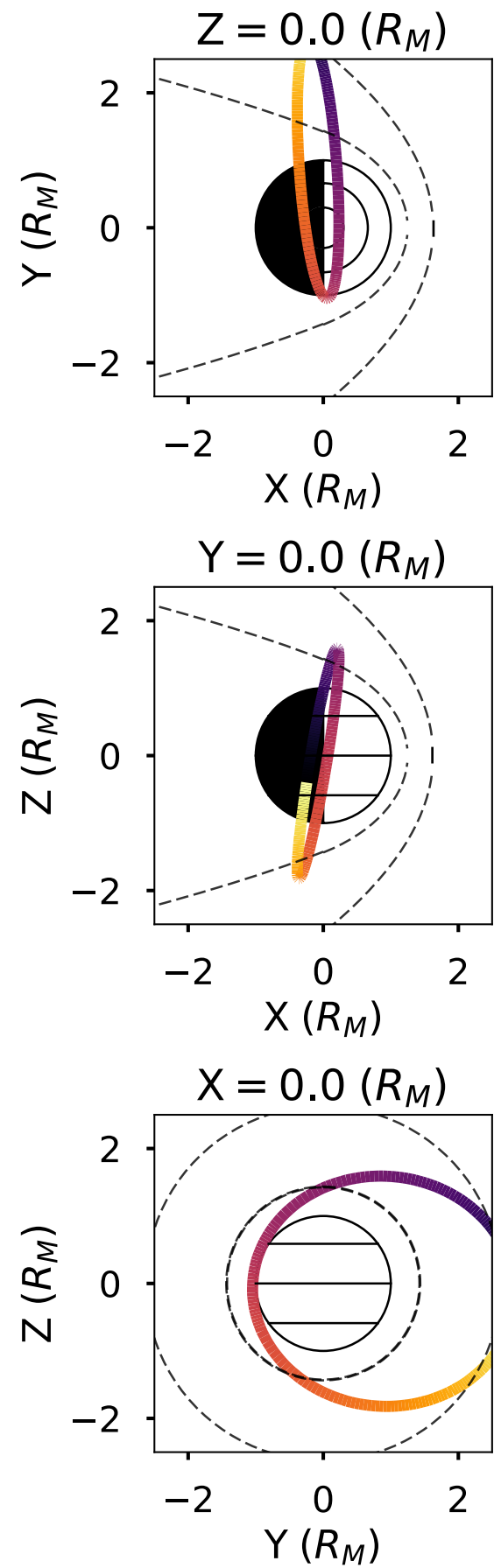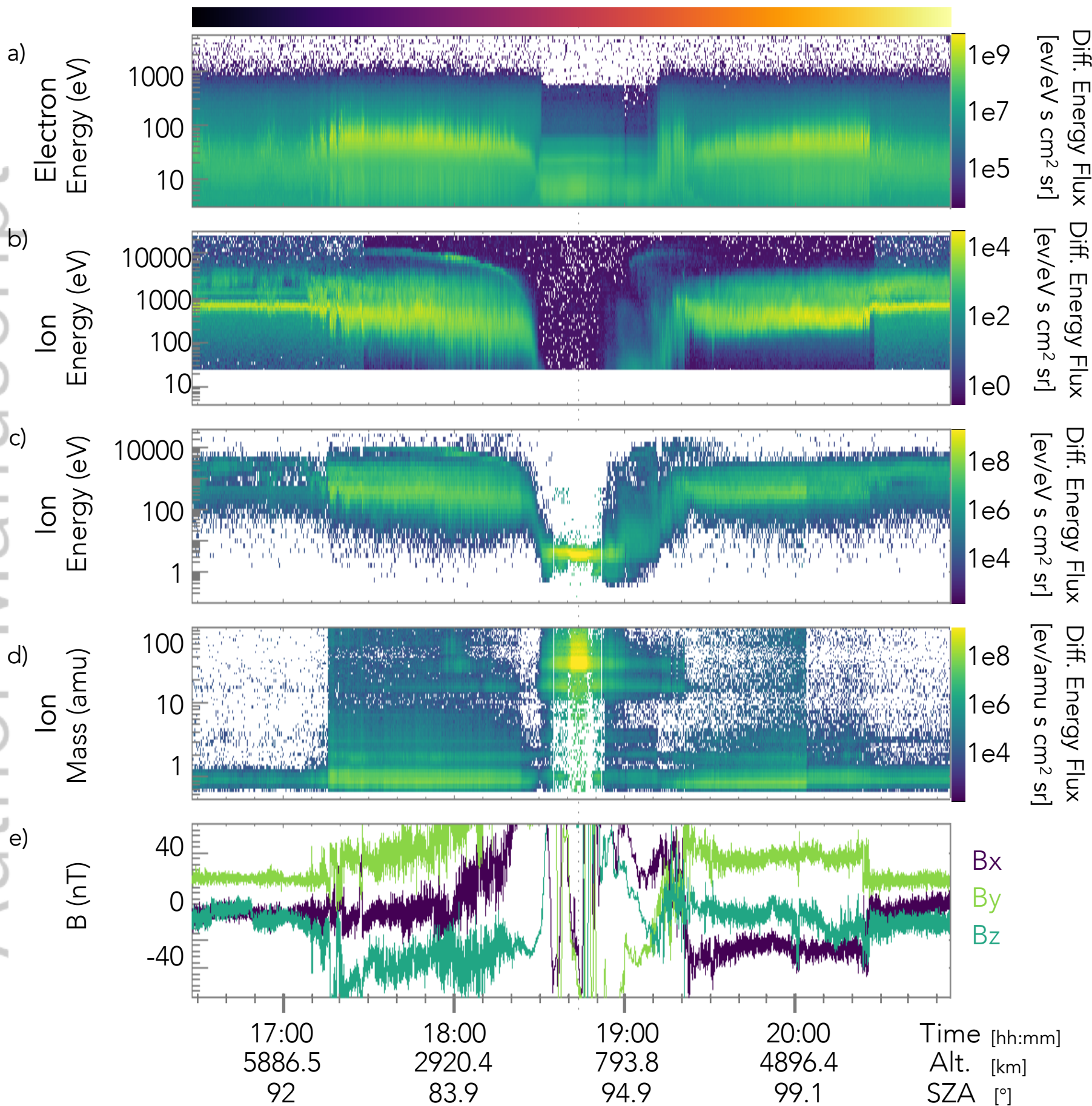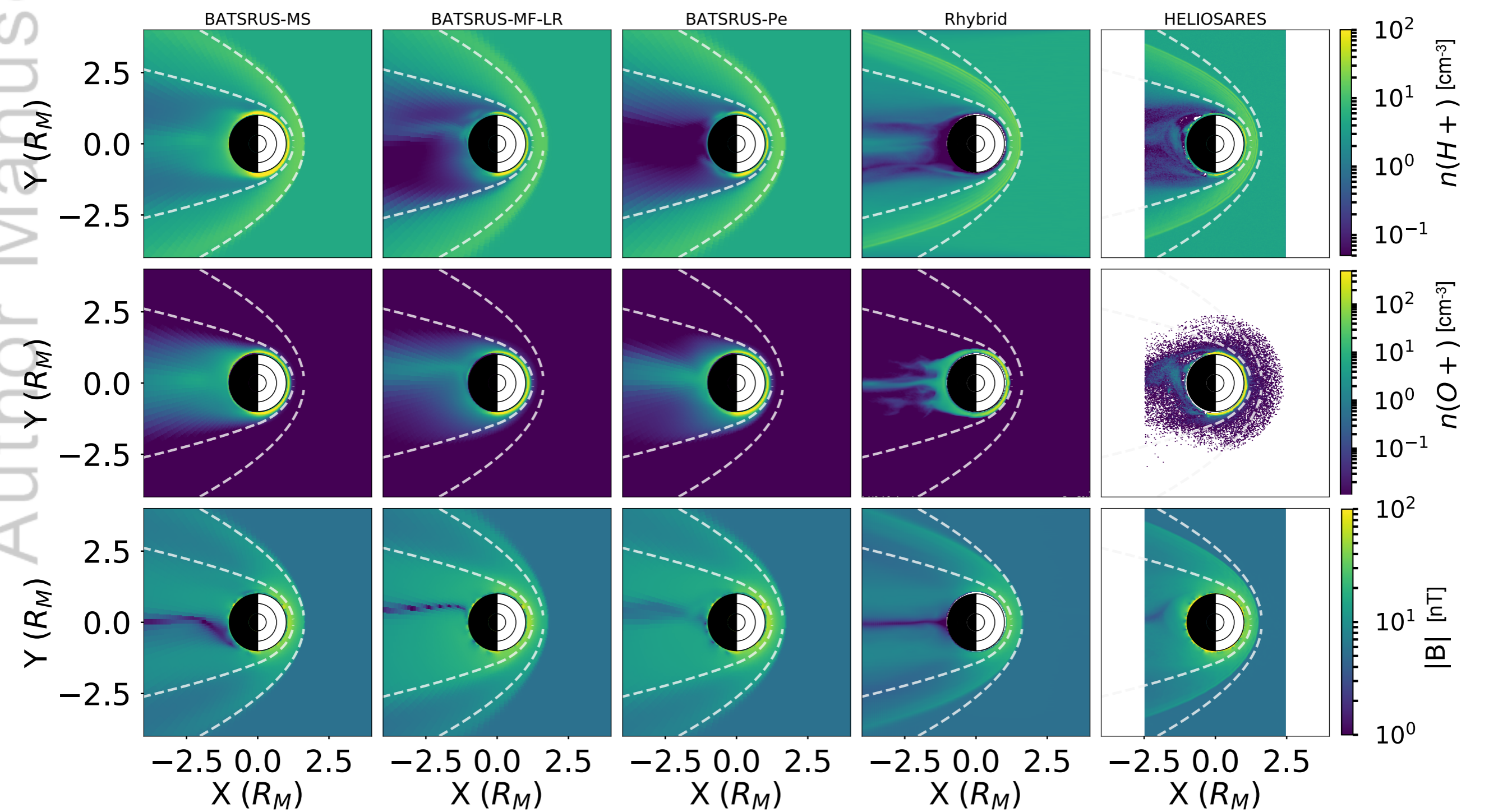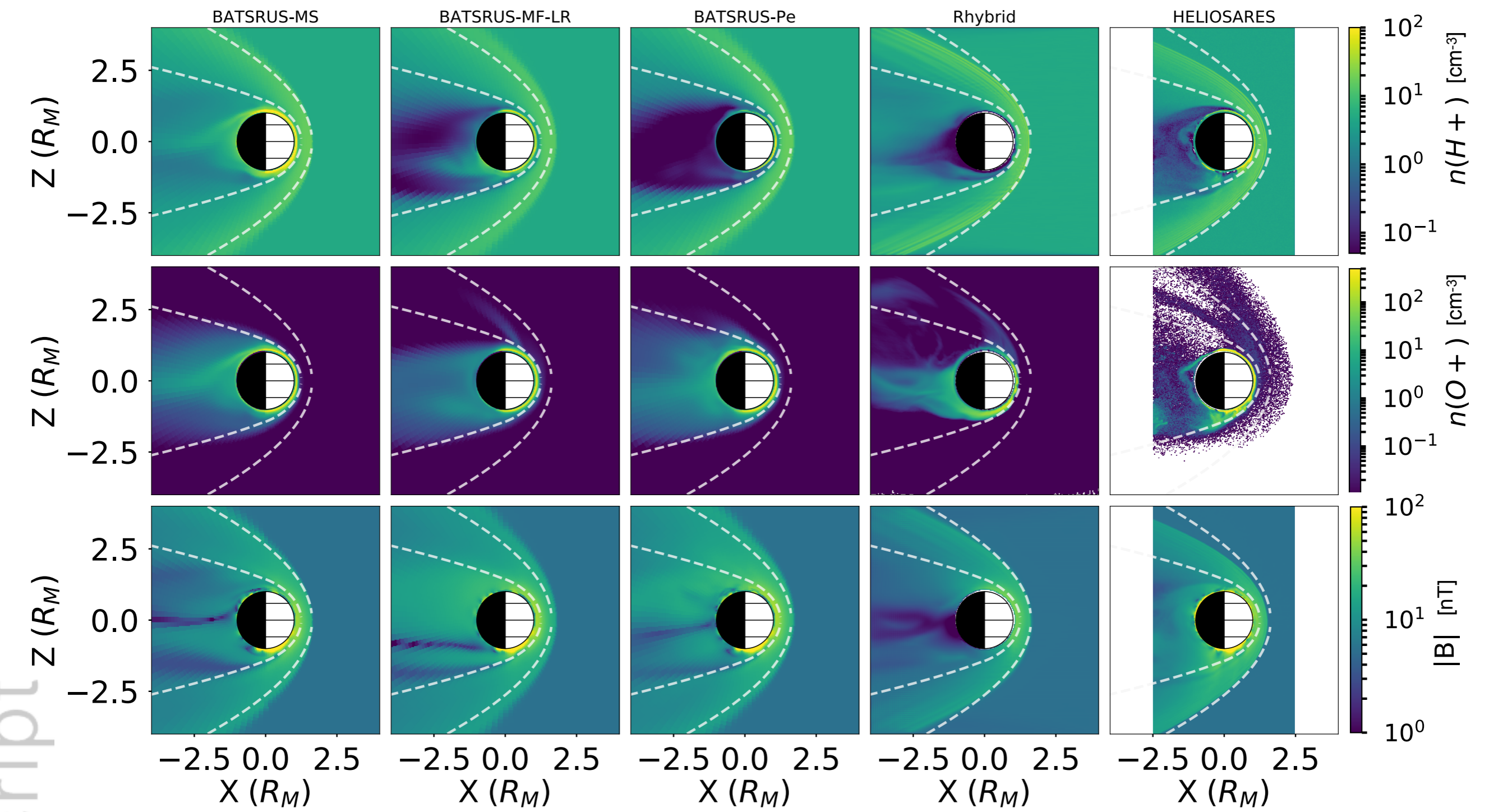
2.

Figure 3.

Figure 4.

Figure 5.

Each column panel is labeled at top: Z = 0.0 (R_M), Y = 0.0 (R_M), X = 0.0 (R_M)

Axis labels (top row): X (R_M), Y (R_M)
Axis labels (middle row): X (R_M), Z (R_M)
Axis labels (bottom row): Y (R_M), Z (R_M)

Colorbar label: n(O+) [cm^{-3}]
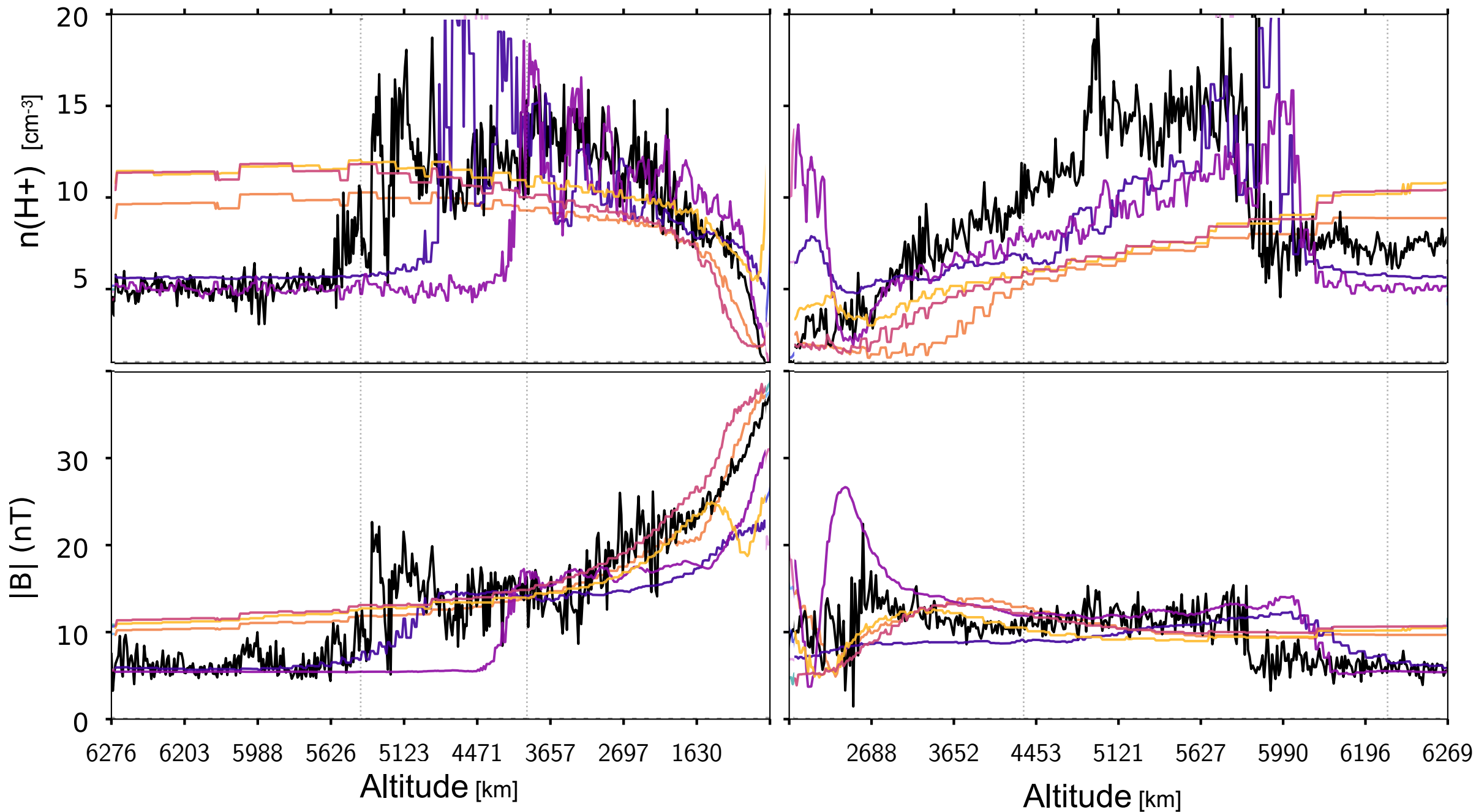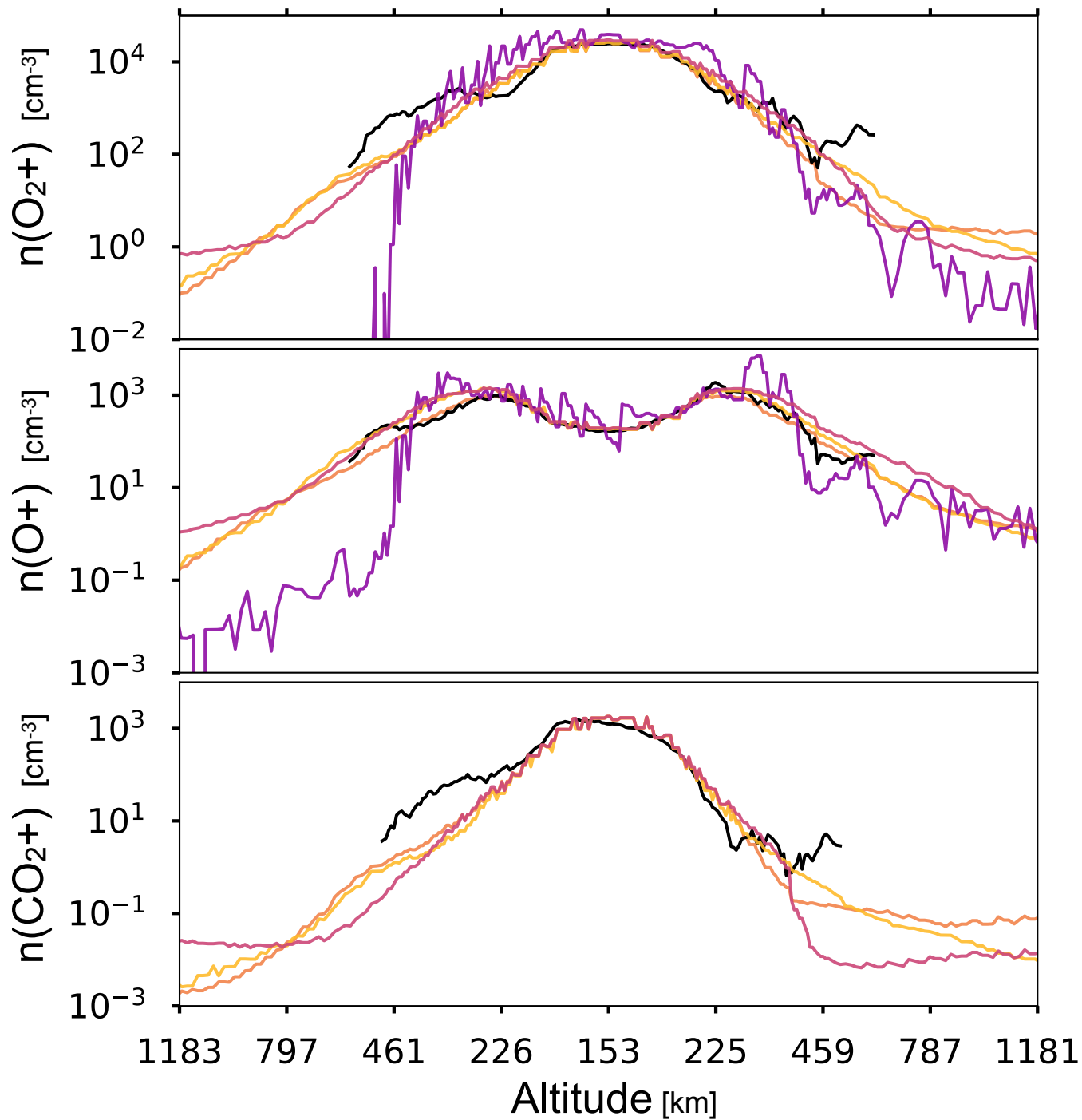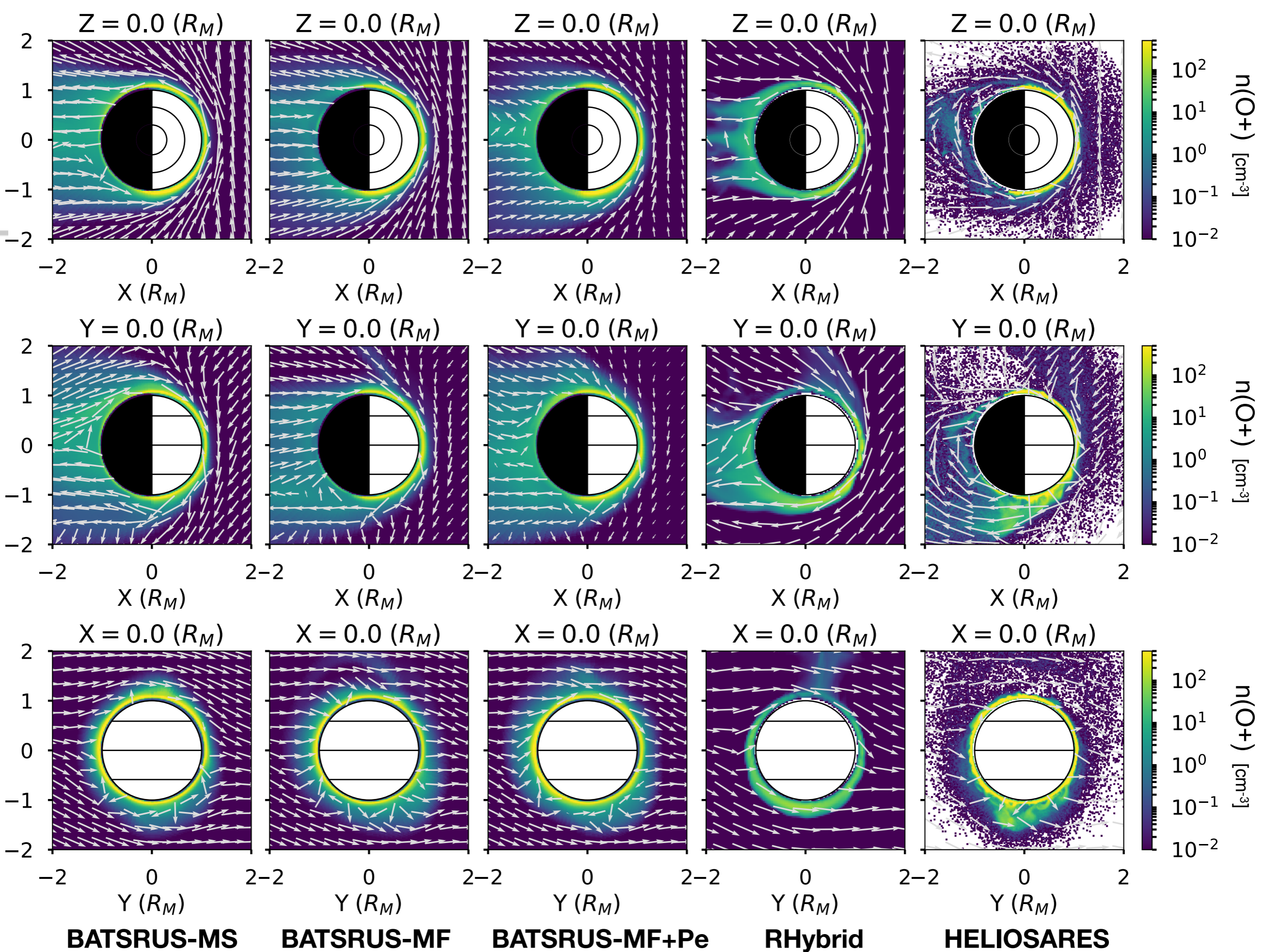
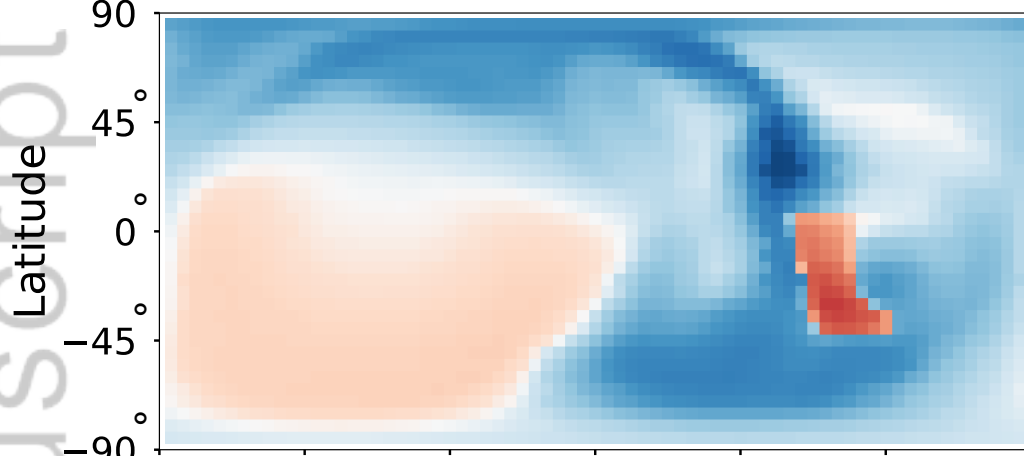Column labels: **BATSRUS-MS**   **BATSRUS-MF**   **BATSRUS-MF+Pe**   **RHybrid**   **HELIOSARES**
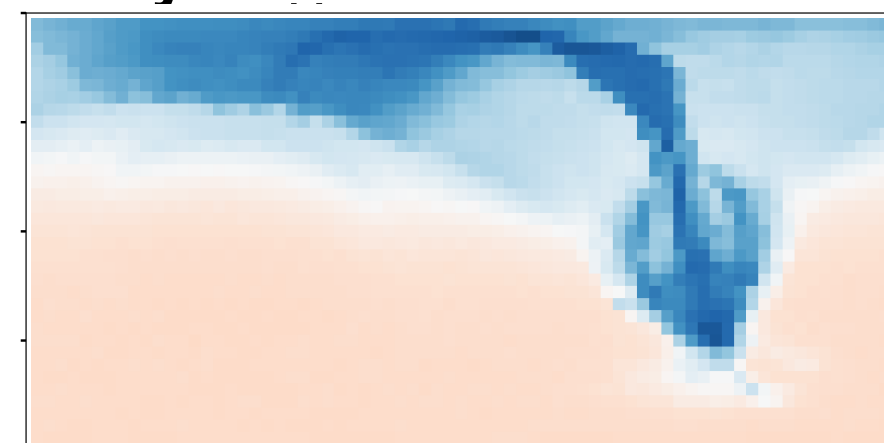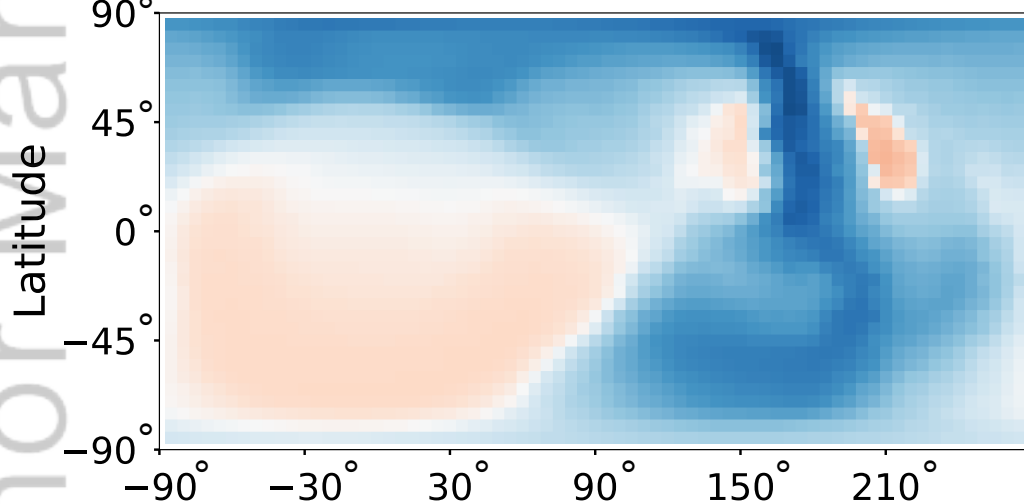
Figure 6.
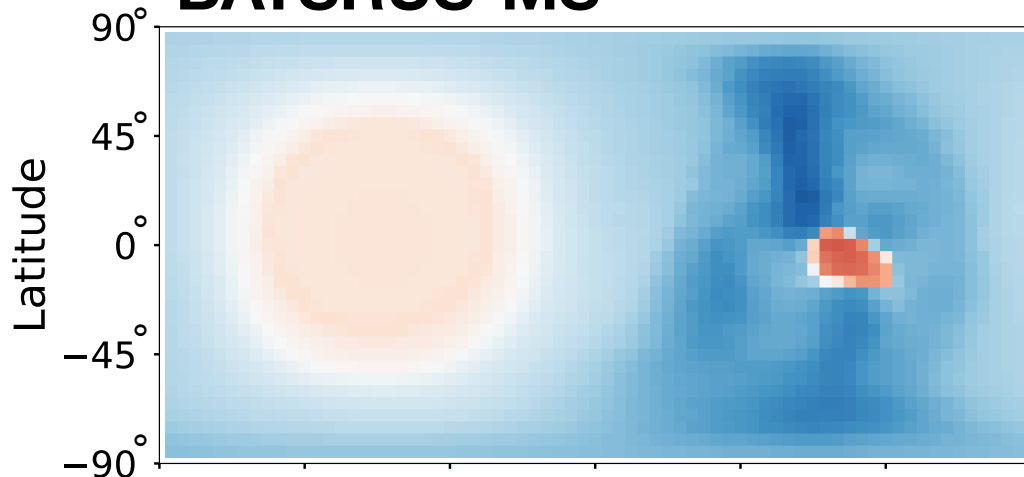
BATSRUS-MS

HELIOSARES
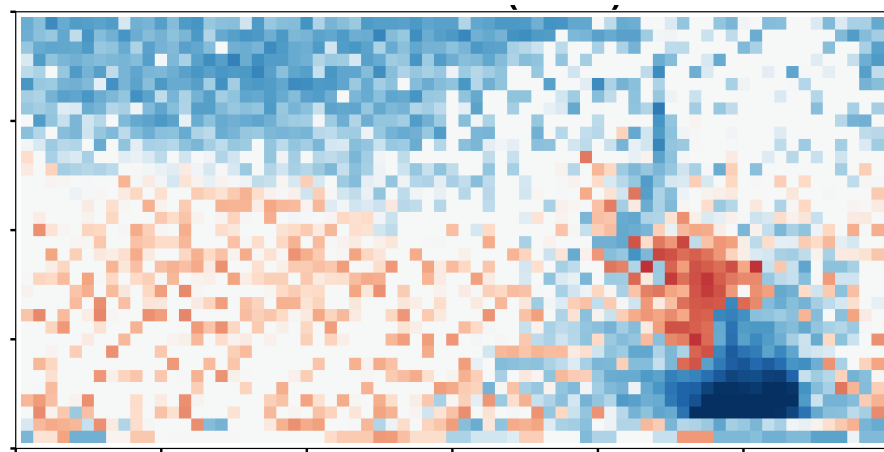
BATSRUS-MF

RHybrid

BATSRUS-MF+Pe

MAVEN

Latitude

Longitude (0=Dayside, 180=Nightside)

Longitude (0=Dayside, 180=Nightside)

Total Ion Flux [#/cm²s]